

Reviewer comments (in blue), our response (in black), revised text (in orange)

Reviewer #2 comments:

1) I have a few concerns regarding the setup and representativeness of laboratory experiments.

First, Figures 1 and 2 are misleading because the authors show selected alpine rock walls and related temperature time series.

We changed Figures 1 and 2 completely and created a new Figure 1 focusing on experimental setup, samples, and applied temperature cycles.

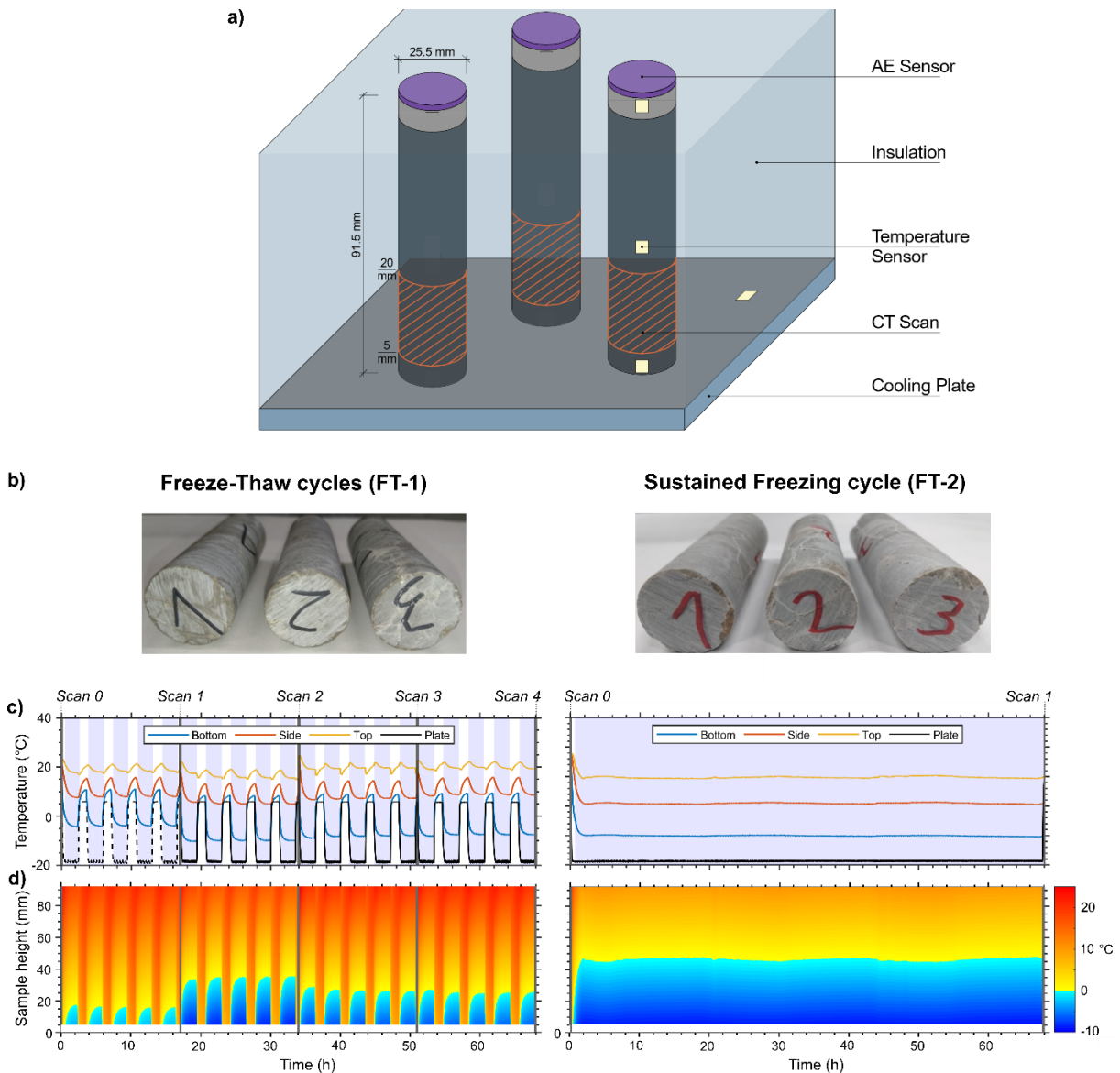


Figure 1: The design of the experiment was influenced by the methodologies of Hallet et al. (1991) and Mayer et al. (2023), focusing on distinguishing ice segregation as a distinct weathering process from other weathering mechanisms. a) Schematic representation of freezing laboratory setup. We created a linear temperature gradient by cooling three rock samples, each with varying levels of saturation, using a cooling plate positioned at the bottom, while exposing the top of the samples to ambient room temperature conditions. b) 91.5 x 25.5 mm large cylindrical Dachstein limestone samples used for freeze-thaw experiments. c) temperature cycles were implemented for FT-1 and FT-2, along with the

corresponding measurements of rock and cooling plate temperatures. In FT-1, between scan 0 and 1, there was inadequate coupling of the temperature sensor, resulting in excessively high temperature readings. d) temperature isoplots of derived temperature distribution within the sample.

Still, the thermal conditions in the laboratory experiments do not correspond to reality (neither the gradients nor the duration, which are, besides the water availability, crucial for ice segregation).

We deviated from highlighting rockwall conditions in our experimental runs and added in the text: 'With this setup we simulated an closed system that provides a linear temperature gradient and a water body inside the rock samples reflecting simplified natural rockwall conditions.'

Further, the timely changing thermal conditions (i.e., periods with non-linear temperature gradient in the sample) driven by the cooling plate at the bottom are not adequately considered (no uniform temperature gradient from bottom to top and lateral temperature gradient from inside to outside are ignored).

We added in Fig1 d the isoplots for both experimental runs (see above) to show temperature dependencies of the samples. We also added in the method section a more critical statement: 'The surface temperature of the sample has a slight offset compared to the internal temperature at the center, with lower temperatures in the core of the sample. However, we assume this offset as minor due to the high thermal conductivity of limestone ($2.4 \text{ Wm}^{-1}\text{K}^{-1}$ (Cermák and Rybach, 1982).'

Second, the number of samples is minimal (only 1 sample/experiment for each condition), does not allow such firm conclusions, and certainly not for a direct implication to the real world.

We weakened our conclusions and fully deleted section 4.4 with interpretations of our findings onto rockwalls. We critically stated the results about saturation impact as sample number was low and saturation levels did change over the experiment. Method Section: 'As saturation influences frost weathering, we used rock samples with an initial saturation of approximately 30, 70 and 100 % categorized as low, partially, and highly saturated, respectively. The samples were saturated by immersing the lower part into a distilled water bath. To prevent air inclusions, we raised slowly the water table until samples were completely immersed, and a constant mass was prevailing (we refer to as highly saturated). Subsequently, samples were dried under atmospheric conditions, weighed until low (30 %) or partially saturation (70 %) was reached. To minimize moisture loss through evaporation, the samples were wrapped in clingfilm. As porosity of the samples is 0.1 %, the level of saturation is inaccurate and provide only a rough estimation. Furthermore, the saturation can change during the experiments due to moisture loss or distribution of rock moisture can alter within the rock samples. We chose the length of the rock samples of 91.5 mm to enable moisture migration towards the sample parts close to the cooling plate where freezing occurred. Due to the low number of samples, we cannot quantify saturation effects on frost weathering, however, our set up enables us to incorporate the ariability of saturation levels occurring in natural rockwalls and to test the consistency frost damage patterns.'

Still, our results highlight that all samples showed the same dependency between initial crack density and crack growth. We can also conclude that all samples of FT-1 showed a higher crack growth compared to FT-2.

Discussion section: ‘Based on μ CT data, freeze-thaw cycles (FT-1) revealed higher rock damage compared to a sustained freezing-cycle (FT-2) in low-porosity crack-dominated alpine rocks. Final crack growth is affected by initial crack density or pore volume distribution and cannot be compared directly; however, normalized crack growth fraction revealed an increase between 29 and 52 % for FT-1 compared to an increase between 2 and 12 % for FT-2 (Fig. 6a, d). The increase varied between samples of different saturation levels. While the low number of samples prohibit a quantitative analysis of saturation effects on rock damage, our results are consistent and reveal higher damage of FT-1 compared to FT-2 independent of saturation levels (Fig. 6a, d).’

Third, the coupling between the AE sensor and the rock is crucial, but there is no proof of how good it is and if it is comparable between the experiment's start and end. For example, how do you explain the change in the yellow slope in Figure 4c?

We did measure coupling with lead break tests before and after the experiment. We added in the text: ‘We performed lead break tests as sample cracks (Eppes et al., 2016) before and after each scan to control sensor coupling and evaluating system performance and wavelength form. Poor coupling of an AE sensor could lead to diminished AE amplitudes, meaning signals of low amplitude might not be detected by the system. To avoid erroneous AE signals stemming from the setup, the system underwent testing without any freezing or temperature alterations.’

We stated a potential coupling shift in the results section:

‘Throughout the cycles, a pattern of accumulating AE hits among the samples is evident. Initially, the highly saturated sample accumulated the majority of hits in the first 10 cycles (121 hits). However, there was a notable increase in AE hits for the partly saturated sample, eventually leading to a higher total than the highly saturated sample between 10 and 20 cycles (173 hits). Given the consistent trend observed in both the highly and low saturated samples, a likely shift in the coupling between the AE sensor and the sample is suggested. Consequently, it is probable that the total AE hits for the partly saturated sample were fewer than those for the highly saturated one. Due to two recording interruptions of the AE logger, AE hits for the FT-1 cycle are likely underestimated.’

We critically discussed the change in slope at the yellow line in Figure 4c in the discussion section:

‘A potential alteration in the AE sensor's attachment to the rock might affect also signal detection. Although we reattached sensors and conducted lead break tests during the FT-1 cycle, the connection could have changed over time. Given the consistent AE accumulation trend observed in both the highly and low saturated samples, a likely coupling shift at the partially saturated sample is suggested (Fig. 3e), which was not reflected in μ CT crack growth data (Fig. 5b, h).’

Further, a direct comparison between two AE time series must be interpreted carefully, and the threshold level might need to be adjusted. For example, if you normalized the summed AE hits in Figure 7, I would expect that they all have a similar pattern (repeating in FT-1, comparable even to FT-2). Therefore, at the moment, the AE results are over-interpreted, and a more in-depth evaluation is required.

We utilized the AE Win software to analyse and filter the incoming AE signals, verifying that no adjustment of the threshold was necessary. We stated this in the method section:

‘The detected AE signals were recorded with a Physical Acoustics micro SHM node. Recorded data were subsequently processed and filtered using Physical Acoustics AEwin software. Due to low background

noises of our setup, we set an initial signal threshold of 30 dB_{AE}, which is similar to Mayer et al. (2023) who established a threshold of 35 dB_{AE}, due to the presence of stronger background noises. We performed lead break tests as sample cracks (Eppes et al., 2016) before and after each scan to control sensor coupling and evaluating system performance and wavelength form.'

We critically discussed AE logger results in the discussion section:

'4.1 Critical discussion on AE Monitoring, stress modelling and μ CT technique

Thermal and ice stresses or a combination of these stresses can cause rock damage. We monitored AE as a proxy for cracking as previous stress experiments (Eppes et al., 2016; Hallet et al., 1991) and analysed the timing of AE events in combination with simplified thermal stress and ice stress models to decipher the potential stress source. Our findings indicate a proportional relationship between the number of AE events and rock damage quantified via μ CT (Fig. 6a,d) which was also shown by findings of Wang et al. (2020a). However, in our study the highest count of AE hits does not always align with the most visible rock damage (Fig. 6a). Specifically, the partially saturated sample exhibited over 415 AE hits with a normalized crack growth fraction of 47%, while the low saturated sample displayed 180 AE hits alongside a 53% crack growth. In contrast to our setup, Wang et al. (2020a) utilized a rock sample with artificially created macro fractures that predominantly drove the generation of AE signals. The discrepancy in our results might be due to variations in volume growth per crack propagation, potentially causing fewer AE releases with greater porosity growth. Additionally, the distinct responses of our natural rock samples to stress, influenced by slightly varying rock parameters, crack distribution and saturation, could also impact the number of AE hits. A potential alteration in the AE sensor's attachment to the rock might affect also signal detection. Although we reattached sensors and conducted lead break tests during the FT-1 cycle, the connection could have changed over time. Given the consistent AE accumulation trend observed in both the highly and low saturated samples, a likely coupling shift at the partially saturated sample is suggested (Fig. 3e), which was not reflected in μ CT crack growth data (Fig. 5b, h). Despite these variables, the partially saturated sample showed before the shift already a higher AE accumulation than the less saturated one, underscoring that AE hits did not completely correlate with crack growth.'

We changed figure 7 and normalized the summed AE hits. We simplified our interpretation and focused with AE hits timing and occurrence. We added in the text: 'The setup of FT-1 enables the development of thermal stresses during cooling and warming of the samples, volumetric expansion alongside the expanding freezing front and ice segregation during freezing conditions (Fig. 7a). In addition, FT-2 favours the development of ice segregation when temperatures are sustained and rock moisture is able to migrate towards the freezing front (Fig. 7a).'

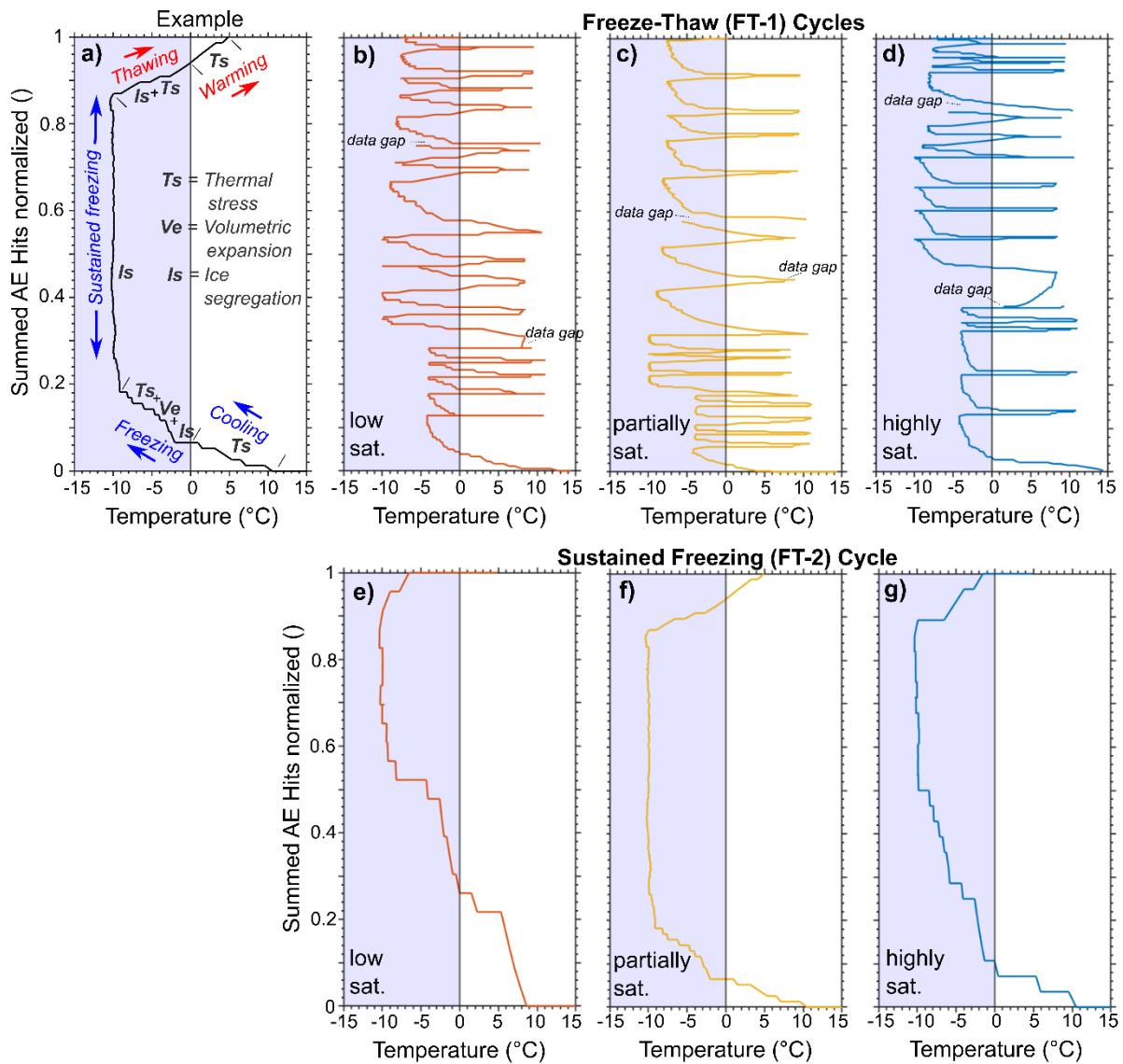


Fig. 7: Cooling phases accumulate more AE hits compared to warming phases, suggesting frost cracking as the main contributor to rock damage. a) Timing examples of potential stress occurrences include thermal stresses during sample cooling and warming, volumetric expansion along with the expanding freezing front, and ice segregation under freezing conditions. Cumulative AE hits are plotted against the bottom rock temperature sensor for b-d) FT-1 and e-g) FT-2.

Fourth, I'm very fascinated by the micro-CT results. I wonder if you saw similar patterns at other locations (e.g., vertically above). Nevertheless, the comparison between the scans seems to be not very sophisticated/quantitative (there are many approaches from photogrammetry for quantifying changes ...).

We followed state of the art procedure in μ CT analyses which was also done by Cnudde and Boone (2013). We modified the methodology sections to enhance comprehension and introduced a new figure, further contributing to a clearer understanding.

'All subsequent image handling, such as registration, segmentation, and analyses, were performed with Avizo3D Pro (Version 2021.1, ThermoFisher Scientific). In Avizo, a sandbox filter was conducted to bin contrast variations inside the images and match contrast between the single scans. We tuned the

parameters until visually the best result was observed. Therefore, sample voids (pore space) and matrix (sample material) of each image could be separated by thresholding over contrast. We followed the work after Deprez et al. (2020a) and defined a distinguishable feature in the scan image as a minimum spatial resolution of 3 times the voxel size (60 μm). Volume fractions and the expansion of pore space in the sample were assessed using photogrammetry in Avizo. For each image, the software detected and quantified distinctions between void voxel V_V and the matrix voxel V_M which we call crack fraction cf (Fig. 2b). Crack fraction is derived by:

$$cf = \frac{V_V}{V_V + V_M} \quad (1)$$

This approach enabled subsequent comparisons between scans to assess the development of pore space growth in the sample (Fig. 2c,d). The parameter crack fraction was defined by the total amount of segmented pore space (voids) per image in the image stack (cross section) divided by the total amount of segmented sample material (matrix + voids). Due to effects of beam hardening, which result in image distortion at sample heights between 0 and 5 mm and between 19 and 20 mm, our analyses were concentrated on the portion of the rock sample ranging from 5 to 19 mm in height. We quantified crack growth (pore space growth) by comparing the crack fraction per layer after each scan (Fig. 2d and 6a-f).

If growth occurs in every crack or void, this implies that the distribution of initial cracks/voids could either accelerate or decelerate the growth of cracks. Consequently, crack growth cannot be directly compared across samples due to variations in crack distribution. To address this, we adjusted each scan cf_i by its initial crack fraction cf_0 , allowing for an assessment of crack growth that is independent of the initial crack distribution. The normalized crack fraction, cf_{norm} for each scan is calculated as follows:

$$cf_{norm,i} = \frac{cf_i}{cf_0} \quad (2)$$

where i represents the scan number. For the purpose of assessing the progression of quantified frost damage both within a single sample and among different samples, we computed the mean of cf_{norm} for each scan.

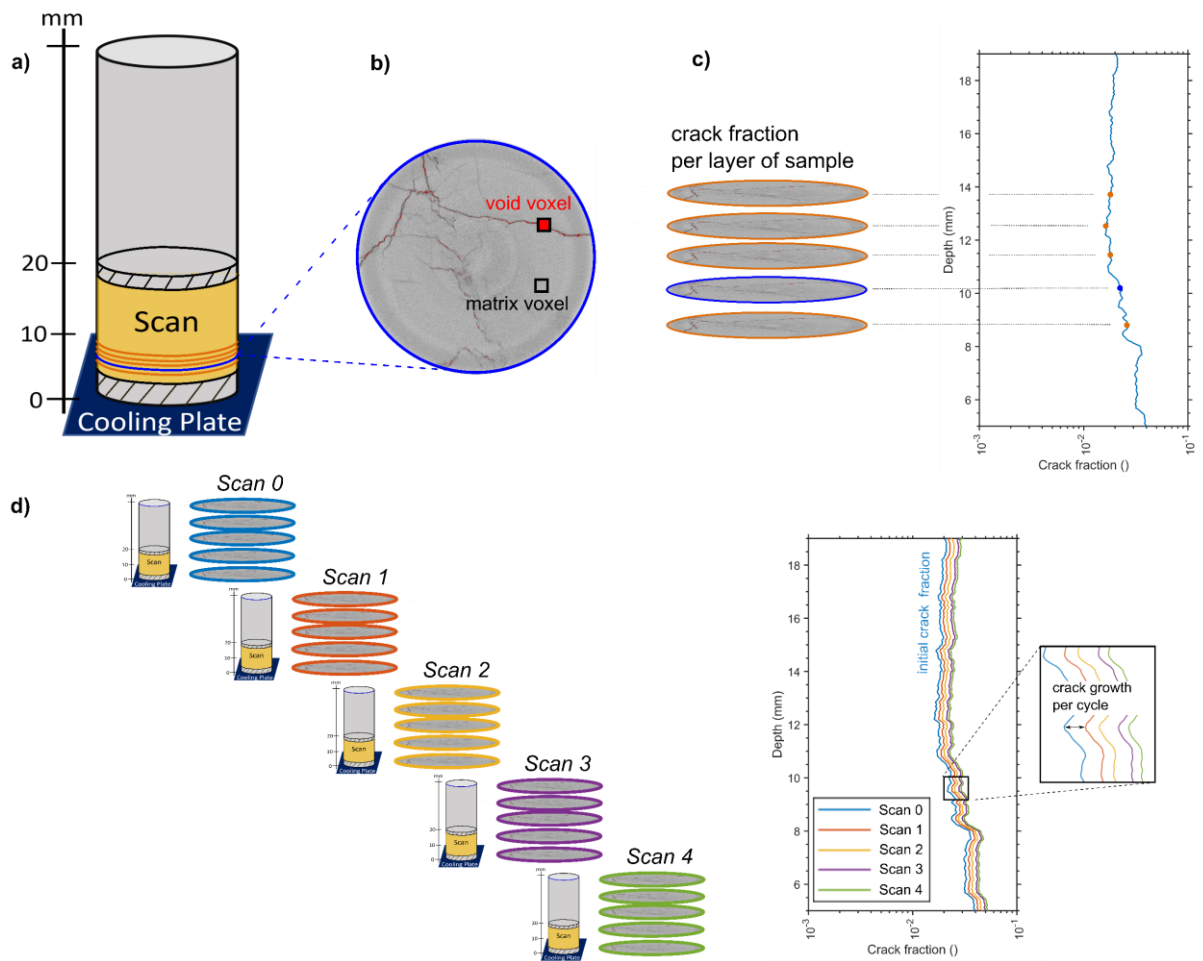


Figure 2: Schematic drawing from scan to crack growth. a) scanned volume from 0 – 20 mm sample height. Due to beam hardening effects (black dashed area) at the edges only the area between 5 - 19 mm sample height was analysed. b) Example scan of one layer (20 μm thick) with example void/crack voxel and matrix voxel derived by Avizio3D Pro. c) Crack fraction derived for each layer over the whole scanned height from 5 - 19 mm by photogrammetry. d) Example of resulting crack growth per cycle with initial crack fraction (blue line).

We also edited Figure 5 for a better understanding of our results.

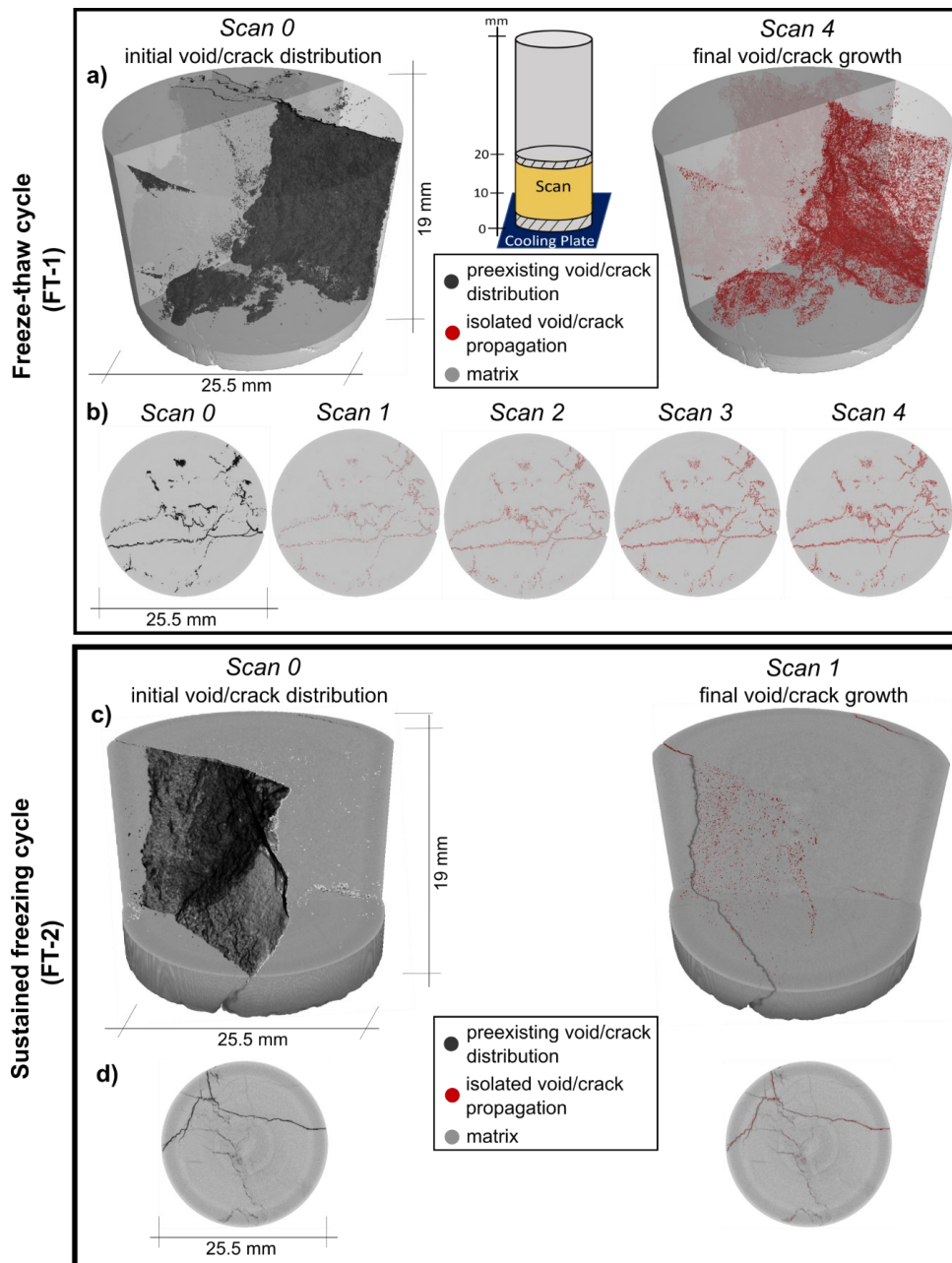


Figure 4: μ CT visualizes crack growth at both cycles FT-1 and -2. a) 3D CT scans before (scan 0) and after the last freeze-thaw cycle (scan 4) of low-saturated rock sample experiencing FT-1 and c) partially saturated rock sample. The initial distribution of cracks/voids is depicted in black, whereas red illustrates solely the isolated growth of these cracks. Example CT scan slices at 8 mm height from the bottom for b) the low saturated sample exposed to FT-1 and d) for the partially saturated samples experiencing FT-2.

Regarding your comment: 'Fourth, I'm very fascinated by the micro-CT results. I wonder if you saw similar patterns at other locations (e.g., vertically above).' In the scanned section of the sample (5 to 19 mm sample height) we did find similar patterns which can be seen in the following figure.

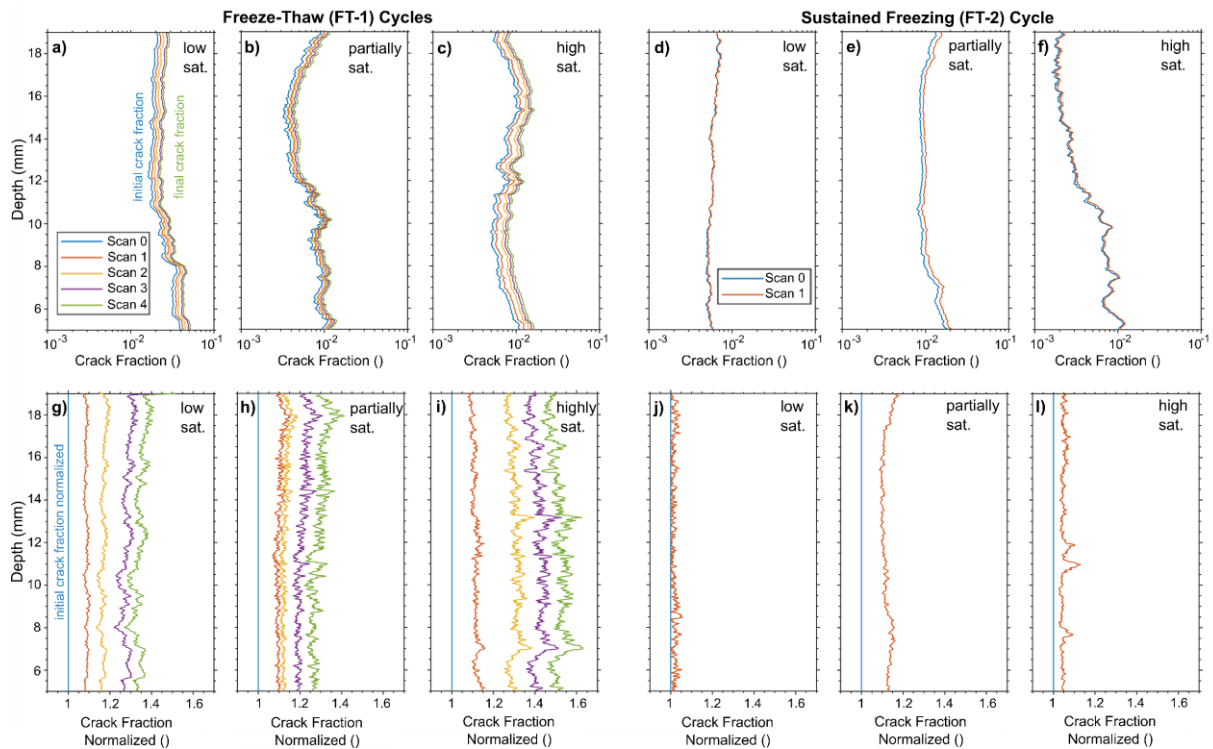


Figure 5: μ CT effectively showcases the progression of cracks in our samples, illustrating a steady growth in crack volume that is uniform throughout different heights in the sample and directly correlates with the initial crack volume. a-f) Measured crack fraction (volume of cracks/voids divided by total volume, refer to Fig. 2b) using μ CT plotted against rock depth. g-l) Quantified normalized crack fraction by initial crack volume (blue line a-f) plotted against rock depth.

Fives, how do you assess the scalability and transferability to real-world conditions? There is no critical discussion on this with consideration.

We removed Discussion 4.4 and introduced a new discussion that critically examines the implications of our findings.

‘4.4 Implications for alpine rockwalls

Our results revealed that the presence and arrangement of voids and fractures within rock significantly impact frost damage. We have shown that micro-crack expansion tends to follow pre-existing fractures, extending their width and length (Fig. 4 and 5g-l), leading to a gradual increase in crack size. As a result, samples with a higher crack density experience more severe frost damage. In natural rockwalls, both micro and macro cracks are present, the latter often arising from tectonic forces and/or weathering effects. These fractures play a crucial role for erosion processes as they influence rock cohesion and modify the dynamics, patterns, and locations of geomorphic activities on various spatial and temporal scales (Scott and Wohl, 2019). Studies by Hales and Roering (2009) and Draebing and Mayer (2021) have established a link between frost cracking intensity and the density of fractures, with rockwalls exhibiting more fractures also showing greater evidence of frost cracking. Furthermore, Eppes et al. (2018) have demonstrated through both field and laboratory observations that an increase in the length and quantity of cracks leads to higher long-term erosion rates. Neely et al. (2019) revealed that higher fracture density decreases steepness of cliffs and increases catchment erosion rates. In New Zealand, Clarke and Burbank (2010) showed that bedrock fracturing by geomorphic processes including weathering controls the depths of erosive processes as bedrock landsliding. We infer that upscaling our

findings from micro to macro cracks highlights the connection between erosion and fracture density. However, such extrapolation must consider the scale dependencies and complex fracture interactions influenced by broader geological and environmental factors, including tectonic forces, weathering effects, and variations in material properties, which could significantly modify erosion dynamics beyond micro-scale observations.

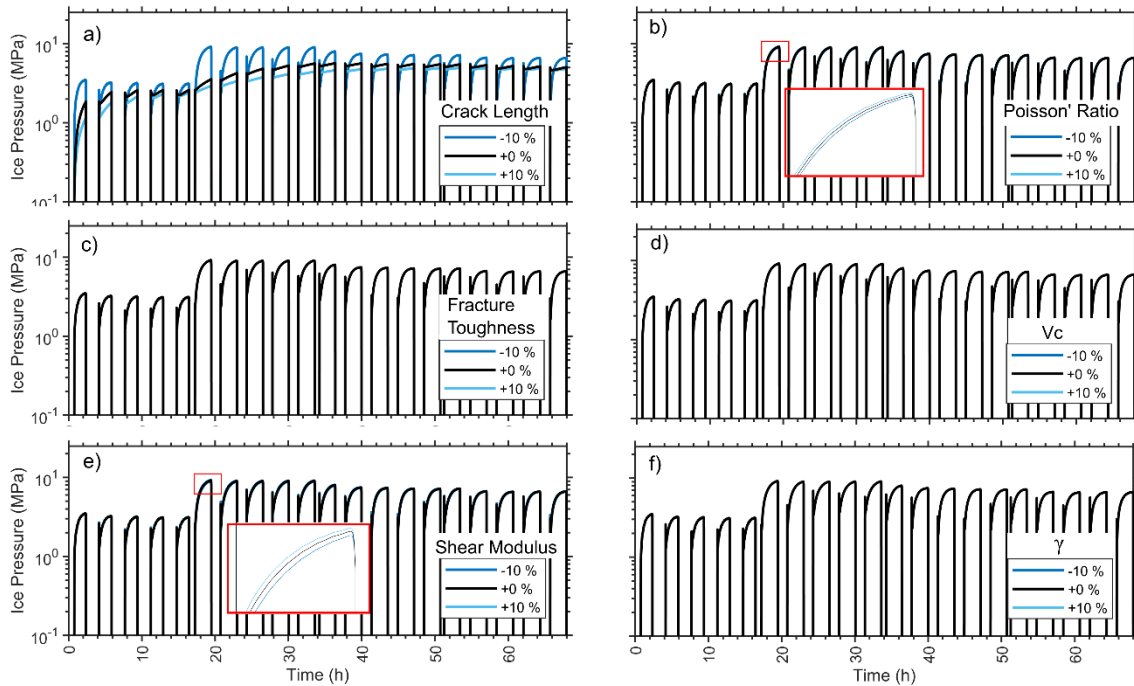
Our findings indicate that frost cracking is more effective during freeze-thaw cycles than during prolonged periods of freezing. Matsuoka et al. (1998) indicated that south-facing rockwalls typically undergo more freeze-thaw cycles due to lack of snow cover, whereas those facing north are subject to longer durations of freezing. This leads to the initial assumption that south facing rockwalls would sustain more frost damage, contributing to increased erosion. However, few existing empirical data indicates that erosion rates are actually 2.5 to 3 times (Sass, 2005a) or up to one magnitude (Coutard and Francou, 1989) higher on north-facing rockwalls. Matsuoka et al. (1998) suggested that while freeze-thaw cycles can cause shallow frost damage (up to 0.3 m deep), prolonged freezing can result in more significant frost damage (up to 5 m deep), leading to larger rockfalls. This indicates that the temporal scale of freeze-thaw cycles plays a crucial role in determining weathering and erosion rates, a concept further supported by Matsuoka (2008), who found that short-term freeze-thaw cycles cause minor crack expansion, whereas long-term freezing leads to more substantial crack widening.

Our research suggests a direct correlation between the frequency of AE events and the extent of rock damage, as measured by micro-CT scanning. However, the highest occurrences of AE hits do not consistently correspond to the most significant observable rock damage. This discrepancy could be attributed to ice formation influenced by thermal gradients, as well as changes and aging in the ice, as discussed by Gerber et al. (2023). This insight has implications for studies that employ AE as an indicator for thermal stress-induced cracking (Eppes et al., 2016; Collins et al., 2018) and frost cracking (Amitrano et al., 2012; Girard et al., 2013) in natural rockwalls.

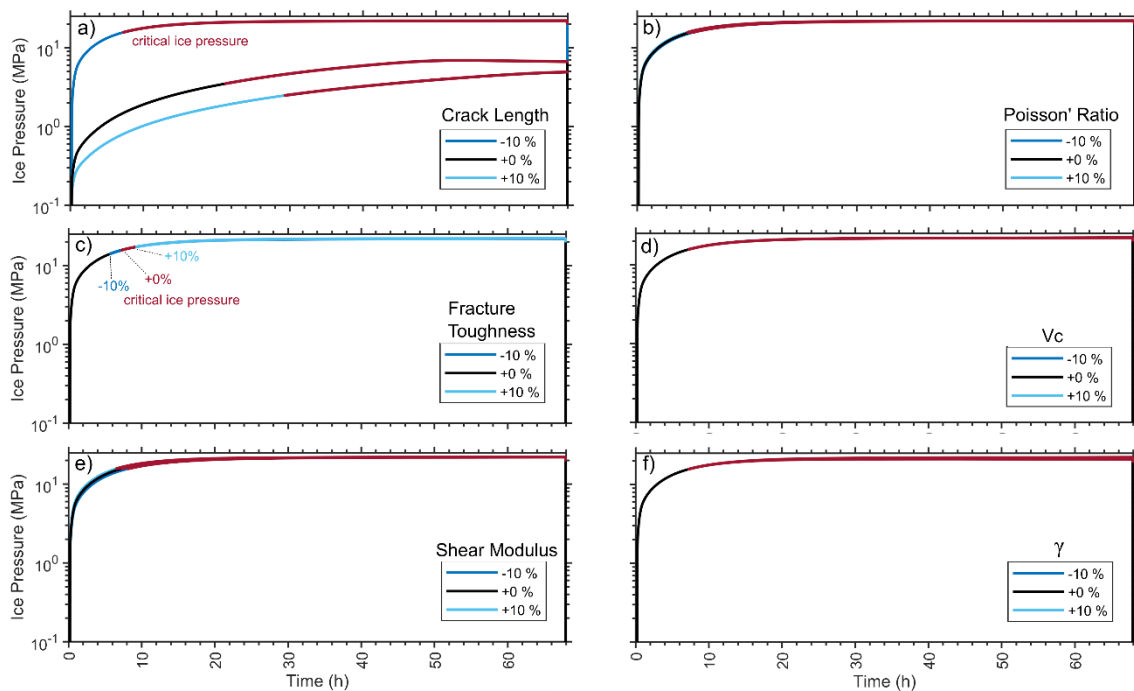
The estimated ice stresses in our simulations may significantly diverge from the actual ice stresses experienced, leading to differences between simulated ice stresses and observed rock damage, particularly in the FT-2 scenario. This mismatch between model predictions and actual frost damage observations could stem from the model's oversimplified representations of crack geometries and rock properties, or the relatively brief duration of sustained freezing in FT-2 when compared to conditions on a real rockwall. Research efforts such as those by Draebing and Mayer (2021) or Sanders et al. (2012) which utilize frost cracking models to assess frost damage, might have overemphasized the effects of frost weathering. Nonetheless, Draebing et al. (2022) showed that frost weathering simulations do correspond with the erosion rates observed on north-facing rockwalls, where extended periods of freezing are more common. ‘

2) The frost-cracking model strongly depends on parametrization and assumptions. Please make a sensitivity analysis, allowing you to visualize the output probabilistically. Publishing the code would certainly give more confidence in the model – I strongly recommend it!

In the Supplementary Information, we included a sensitivity analysis and provided a discussion on it. We altered the values by 10% to observe the impact on the model predictions for FT-1:



For FT-2:



We added a critical discussion in the discussion section:

‘Our approach to model thermal stress did not account for the complex geometries of the cracks in the samples. As a result, our analysis concentrated on the timing of thermal stresses rather than their precise magnitudes. In our frost cracking modelling, we presented results for ellipsoidal cracks starting at a length of 1 mm. It is important to note, however, that cracks vary in size and exhibit more intricate geometries as seen by μ CT imaging (Fig. 4). Additionally, slight variations in mechanical and elastic properties may occur since parameters were derived from different boulders of the same lithology or

were based on data from Walder and Hallet (1985). Our sensitivity analysis (see Supplementary S1 and S2) for frost cracking models revealed that the timing of increasing ice pressure was largely consistent across variations in parameters such as fracture toughness, growth law parameters, shear modulus, and Poisson's ratio. Nevertheless, the crack length significantly influences the timing and the critical threshold for cracking. A larger crack length results in lower and delayed ice stresses, as well as a reduced critical threshold.'

The link to our code will be shown in the data availability section:

Code for frost cracking modelling is available at:

https://github.com/TillM90/Code_frost_cracking_model.git

3) The readability of figures is limited due to resolution, font size, line width, and color scheme. Further, I strongly recommend highlighting the key information in the graphs or mentioning it at least in the caption.

We highlighted the key information in the caption:

'Figure 1: The design of the experiment was influenced by the methodologies of Hallet et al. (1991) and Mayer et al. (2023), focusing on distinguishing ice segregation as a distinct weathering process from other weathering mechanisms. a) Schematic representation of freezing laboratory setup. We created a linear temperature gradient by cooling three rock samples, each with varying levels of saturation, using a cooling plate positioned at the bottom, while exposing the top of the samples to ambient room temperature conditions. b) 91.5 x 25.5 mm large cylindrical Dachstein limestone samples used for freeze-thaw experiments. c) temperature cycles were implemented for FT-1 and FT-2, along with the corresponding measurements of rock and cooling plate temperatures. In FT-1, between scan 0 and 1, there was inadequate coupling of the temperature sensor, resulting in excessively high temperature readings. d) temperature isoplots of derived temperature distribution within the sample.'

'Figure 2: Schematic drawing from scan to crack growth. a) scanned volume from 0 – 20 mm sample height. Due to beam hardening effects (black dashed area) at the edges only the area between 5 - 19 mm sample height was analysed. b) Example scan of one layer (20 μm thick) with example void/crack voxel and matrix voxel derived by Avizio3D Pro. c) Crack fraction derived for each layer over the whole scanned height from 5 - 19 mm by photogrammetry. d) Example of resulting crack growth per cycle with initial crack fraction (blue line).'

'Figure 3: FT-1 resulted in significantly more AE hits than FT-2, as indicated by thermal stress models but not reflected in frost cracking models where FT-2 showed higher predicted ice stresses. More AE hits were recorded during freezing phases compared to non-freezing ones. a-b) Respectively measured rock and cooling plate temperatures, c-d) recorded AE hits (coloured dots) and cumulative AE hits (coloured lines), and e-f) modelled thermal and ice stresses at bottom temperature sensor plotted against time for FT-1 and FT-2 with AE hits from all samples. The dashed black line highlights cooling plate temperatures according to the controller while black lines indicated measured plate temperature (cooling plate sensor was attached after first 5 cycles). The temperature offset between scan 0 and 1 during FT-1 (a) is a result of poor connectivity of the bottom temperature sensor. Blue backgrounds highlight periods when bottom rock samples were exposed to temperatures below 0 °C.'

'Figure 4: μCT visualizes crack growth at both cycles FT-1 and -2. a) 3D CT scans before (scan 0) and after the last freeze-thaw cycle (scan 4) of low-saturated rock sample experiencing FT-1 and c) partially saturated rock sample. The initial distribution of cracks/voids is depicted in black, whereas red

illustrates solely the isolated growth of these cracks. Example CT scan slices at 8 mm height from the bottom for b) the low saturated sample exposed to FT-1 and d) for the partially saturated samples experiencing FT-2.'

'Figure 5: μ CT effectively showcases the progression of cracks in our samples, illustrating a steady growth in crack volume that is uniform throughout different heights in the sample and directly correlates with the initial crack volume. a-f) Measured crack fraction (volume of cracks/voids divided by total volume, refer to Fig. 2b) using μ CT plotted against rock depth. g-l) Quantified normalized crack fraction by initial crack volume (blue line a-f) plotted against rock depth.'

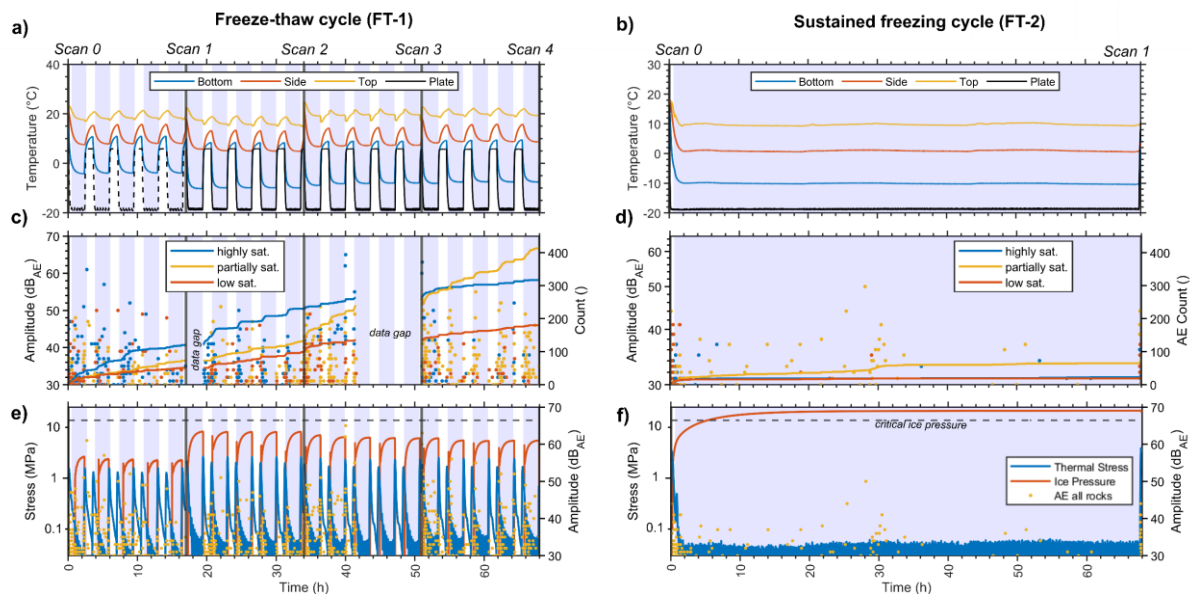
'Figure 6: Freeze-thaw cycles (FT-1) have a higher frost cracking efficacy compared to a sustained freezing-cycles (FT-2) in low-porosity crack-dominated alpine rocks. Normalized crack fraction in relation to accumulated AE hits, simulated summed ice stress and thermal stress for a-c) FT-1 and d-f) FT-2. Simulated stresses by our frost cracking models are higher for FT-2 in comparison to FT-1 which is not aligned by normalized crack fraction.'

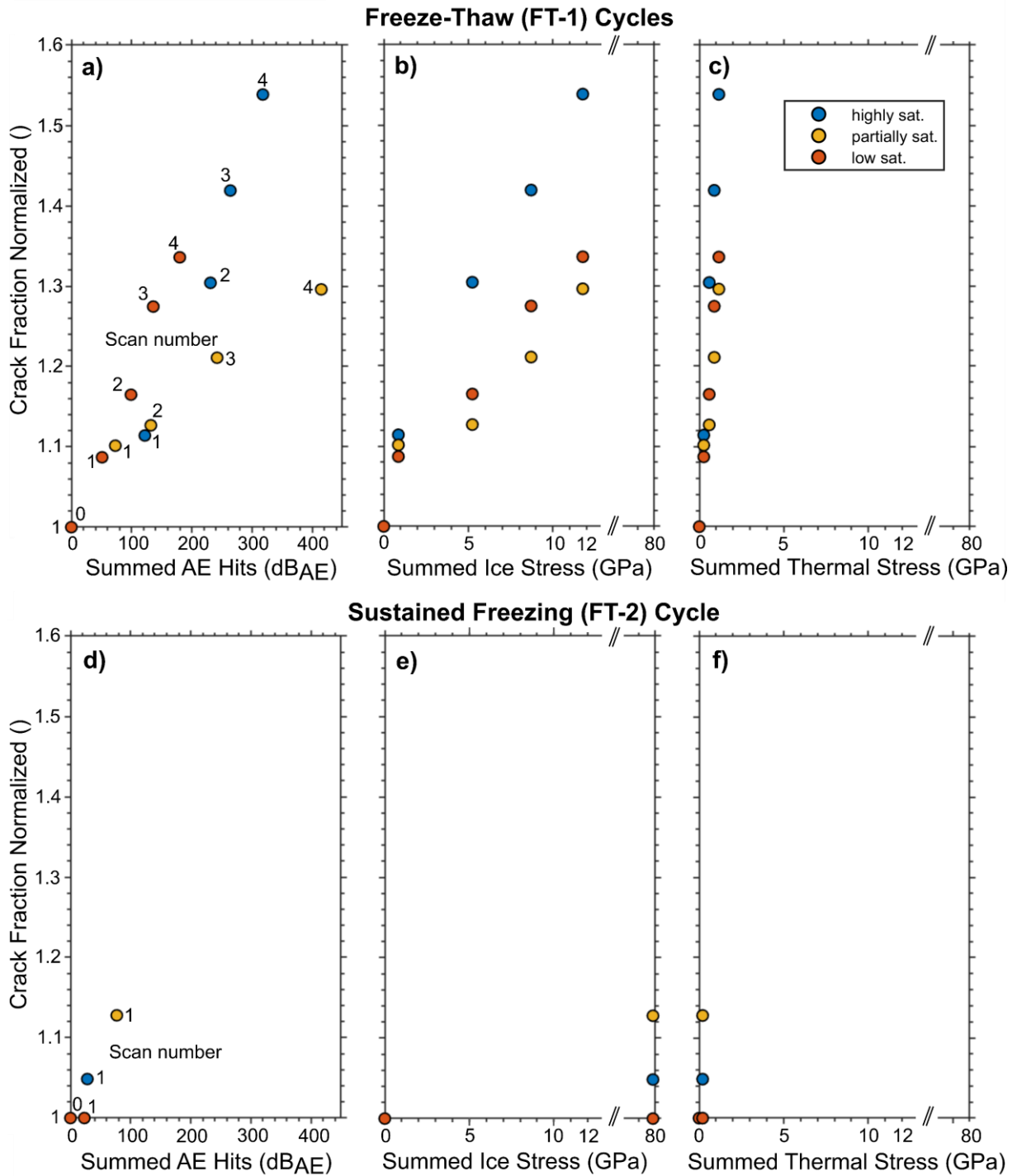
'Figure. 7: Cooling phases accumulate more AE hits compared to warming phases, suggesting frost cracking as the main contributor to rock damage. a) Timing examples of potential stress occurrences include thermal stresses during sample cooling and warming, volumetric expansion along with the expanding freezing front, and ice segregation under freezing conditions. Cumulative AE hits are plotted against the bottom rock temperature sensor for b-d) FT-1 and e-g) FT-2.'

We enlarged the font size across all figures and enhanced the dpi value. The color scheme was selected based on Wong (2011) recommendations, who devised a color scheme that is easily readable by individuals with visual impairments.

Wong, B.: Points of view: Color blindness, Nature Methods, 8, 441-441, 10.1038/nmeth.1618, 2011.

Since most of the figures have already been presented earlier, we will not repeat them here. However, we will introduce the two figures that have not yet been displayed:





4) The manuscript is rather lengthy, especially the introduction. Please reorganize, restructure, and shorten the introduction to avoid repetitions. Section '3 Results' is rather hard to read – please add more explanation and interpretation.

We revised and rearranged the introduction to improve clarity and readability, reducing its length by one third.

'1 Introduction

Frost weathering is a key mechanism for rock breakdown in periglacial environments (Matsuoka and Murton, 2008) and is therefore considered to be the main driver for alpine landscape evolution (Egholm et al., 2015; Hales and Roering, 2009). The breakdown of rock due to freezing is called frost cracking and can prepare and trigger rockfall (Matsuoka, 2019). Cracking can occur when stresses exceed thresholds (critical cracking) or by repetition of low magnitude stresses that progressively weaken the rock (subcritical cracking; Eppes and Keanini, 2017). Frost cracking was associated with two different processes: volumetric expansion and ice segregation (Matsuoka and Murton, 2008).

When water freezes to ice volumetric expansion of 9% occurs and can theoretically build up stresses of up to 207 MPa (Matsuoka and Murton, 2008), which would exceed the tensile stress of most existing rock (Perras and Diederichs, 2014). Conditions that favour volumetric expansion are a high degree of water saturation of 91 % (Walder and Hallet, 1986), a rapid freezing associated with diurnal freeze-thaw cycles (Matsuoka, 2001; Matsuoka and Murton, 2008) and a freezing from all sides (Matsuoka and Murton, 2008). However, conditions facilitating volumetric expansion in real rockwalls are rare as moisture conditions exceeding 91 % are rarely given during phases of rapid freezing (Sass, 2005b).

During freezing processes, ice crystals develop within cracks and pores of rock. A repulsion mechanism ensures that a thin water film (<9 nm) persists between the ice crystal and the walls of the pore or crack (Gilpin, 1979; Webber et al., 2007; Sibley et al., 2021), facilitating the movement of unfrozen water present within the frozen rock matrix towards the ice crystal driven by a thermodynamic potential gradient (Derjaguin and Churaev, 1986; Kjelstrup et al., 2021; Everett, 1961; Gerber et al., 2022). Due to ice segregation, ice expands within pores and cracks and generates crystallization pressure (Scherer, 1999) that can damage rocks. Ice segregation is most efficient in a temperature range called the 'frost cracking window' (Anderson, 1998) which depends on rock strength (Walder and Hallet, 1985; Mayer et al., 2023). Common temperature ranges vary from -6 to -3 °C for low-strength Berea sandstone (Hallet et al., 1991), but can drop to -15 to -5°C for high-strength rocks (Walder and Hallet, 1985; Mayer et al., 2023). Ice segregation can occur in low-saturated rock (Mayer et al., 2023) and is theoretically more conducive in environments characterized by slow freezing rates and continuous low temperatures typical of seasonal freezing (Matsuoka and Murton, 2008; Walder and Hallet, 1986).

Frost cracking serves as an indicator for assessing frost damage or the increase in porosity in rocks and rockwalls, yet its gradual and subcritical nature makes direct measurements challenging. Consequently, laboratory studies have adopted indicators such as AE signals (Hallet et al., 1991; Mayer et al., 2023; Maji and Murton, 2021; Duca et al., 2014), frost heave or crack expansion (Murton et al., 2006; Draebing and Krautblatter, 2019), alterations in mechanical properties like p-wave velocity, Youngs' Modulus, uniaxial strength or porosity (Whalley et al., 2004; Matsuoka, 1990; Jia et al., 2015;

Eslami et al., 2018; Prick, 1997), and frost cracking simulations (Mayer et al., 2023; Murton et al., 2006) to estimate its impact. At the scale of rockwalls, proxies such as AE signals (Girard et al., 2013; Amitrano et al., 2012), fracture density (Hales and Roering, 2009; Draebing and Mayer, 2021; Messenzehl et al., 2018), fracture opening (Draebing, 2021; Draebing et al., 2017b; Draebing et al., 2017a), rockwall erosion rates (Draebing et al., 2022; Matsuoka, 2008), as well as frost cracking simulations (e.g. Draebing et al., 2022; Sanders et al., 2012) have been utilized to infer frost cracking activity. However, all these techniques provide proxies for frost cracking and as low-porosity alpine rocks are characterized by micro-cracks, changes in frost cracking proxies are very small and often within the uncertainty of the techniques used, and therefore do not provide reliable results. In contrast, X-ray computed micro-tomography (μ CT) enables the quantification of material damage (Cnudde and Boone, 2013; Withers et al., 2021) and was previously applied to track frost cracking damage in high-porosity rocks (De Kock et al., 2015; Deprez et al., 2020; Maji and Murton, 2020; Dewanckele et al., 2013) or assess post-experimental frost damage along artificial cracks in low-porosity rocks (Wang et al., 2020a; 2020b) exposed to frequent freeze-thaw cycles.

To our knowledge, no study has directly quantified the effectiveness of different freeze-thaw cycles or demonstrated whether frost cracking creates new cracks or propagates existing cracks in high-strength, low porosity rocks. In this study, we exposed low-porosity, high-strength Dachstein limestone to frequent diurnal and seasonal sustained freeze-thaw cycles during laboratory freezing experiments. We monitor acoustic emission events during the experiments and modelled thermal and ice-induced stresses and applied μ CT to pre- and post-stressed rocks to quantify and track crack propagation and to assess frost cracking efficacy of different freeze-thaw cycles.'

We completely revised the results section to make our findings clearer. We added a short interpretation at the beginning of each results part. Below, we present a portion of the revised results section:

'3 Results

3.1 Continuous AE and temperature monitoring and stress modelling

3.1.1 Freeze-Thaw cycles (FT-1)

The rock samples' bottom was exposed to a temperature range of -19 to 6 °C by the cooling plate. Initial temperature loggers were poorly attached to the rock, causing discrepancies in bottom surface temperatures during the first five freeze-thaw cycles compared to later cycles, as shown in Fig. 3a, suggesting that the actual temperatures were likely lower than those recorded. After five cycles, a temperature sensor was added to the cooling plate. Between freeze-thaw cycles 5 and 20 the bottom rock temperature reached minimal temperatures of -10 to -8 °C and maxima of 8.5 to 9.5 °C, while the top sensor consistently registered 15 to 24 °C.

More AE hits were recorded during freezing phases compared to non-freezing ones (Fig. 3c). The majority of hits occurred when bottom temperatures were below freezing, with the highly saturated sample registering 235 hits, the partly saturated sample 326 hits, and the low saturated sample 123 hits. Positive temperature readings yielded fewer hits: 82 for the highly saturated, 89 for the partly saturated, and 57 for the low saturated samples. Total AE hits observed were 317 for the highly saturated sample, 415 for the partly saturated sample, and 180 for the low saturated sample.

Throughout the cycles, a pattern of accumulating AE hits among the samples is evident. Initially, the highly saturated sample accumulated the majority of hits in the first 10 cycles (121 hits). However, there was a notable increase in AE hits for the partly saturated sample, eventually leading to a higher total than the highly saturated sample between 10 and 20 cycles (173 hits). Given the consistent trend observed in both the highly and low saturated samples, a likely shift in the coupling between the AE sensor and the sample is suggested. Consequently, it is probable that the total AE hits for the partly saturated sample were fewer than those for the highly saturated one. Due to two recording interruptions of the AE logger, AE hits for the FT-1 cycle are likely underestimated.

Our model indicated that both thermal- and ice-induced stresses peaked during freezing temperatures (Fig. 3e). However, due to a temperature discrepancy in the initial five freeze-thaw cycles, the modelled thermal and ice stress were underestimated (Fig. 3e). From the fifth to the twentieth cycle, the highest thermal stresses occurred as temperatures transitioned from thawing to freezing, reaching pressures of 2.15 ± 0.25 MPa and 2.95 ± 0.20 MPa respectively. These stresses were minimal at stable temperatures. Ice stress was present only during freezing, with the model predicting increasing ice stresses up to a maximum of 6.85 ± 1.35 MPa at the end of each freezing phase. This is significantly below the critical ice pressure threshold (13.7 MPa) for subcritical cracking.

3.1.2 Sustained freezing cycle (FT-2)

In the FT-2 run, the partially saturated sample registered the highest number of AE hits, with ice stresses being a major factor. The rock samples underwent 68 hours of freezing, maintaining a constant bottom temperature of -10 ± 0.5 °C (Fig. 3b). During this period, the middle sensor recorded a slightly positive temperature of 0.9 ± 0.3 °C, and the top sensor stayed at 9.8 ± 0.4 °C. AE logging revealed 28 hits for the highly saturated, 77 hits for the partially saturated, and 23 hits for the low saturated sample (Fig. 3d). The fixed freezing phase caused 11 hits to occur at the highly saturated rock, 53 hits at the partly saturated rock and 8 hits at the low saturated rock. Thermal stress modelling indicated peak stresses of 3.6 MPa during cooling and 3.9 MPa during warming at the cycle's start and end (Fig. 3f), dropping below 0.1 MPa at stable temperatures. Ice stress models showed a continuous increase in

ice stress throughout the freezing phase, reaching a maximum of 21 MPa, surpassing the critical ice pressure threshold of 13.7 MPa after 5.4 hours.